

## Article

# Numerical Investigation of Slurry Fracturing during Shield Tunneling under a Reservoir

Bingyu Han <sup>1,2,\*</sup>, Dajun Yuan <sup>1,2</sup>, Teng Wang <sup>1,2</sup> and Zhongxin Wang <sup>1,2</sup>

<sup>1</sup> Key Laboratory of Urban Underground Engineering of the Education Ministry, Beijing Jiaotong University, Beijing 100044, China

<sup>2</sup> School of Civil Engineering, Beijing Jiaotong University, Beijing 100044, China

\* Correspondence: byhan2017@bjtu.edu.cn

**Abstract:** The Jinan Jiluo Road Crossing the Yellow River Tunnel North Extension Project will intersect the Queshan reservoir, which currently supplies 60% of the domestic water in Jinan City. During the excavation process of the large-diameter slurry type shield used in this project, it may lead to slurry fracturing of the stratum in front of the excavation face and slurry blow-out from the surface if the slurry support pressure is too high. The leakage of shield slurry will pollute the reservoir water, and the safety of domestic water in Jinan will be threatened. Shield slurry blow-out may also lead to water inrush accidents. It is difficult to prevent slurry blow-out during shallow shield tunnel construction due to an insufficient understanding of the shield slurry fracturing mechanism. The initiation and extension of shield slurry fracturing are very complex and difficult to observe in the stratum. Currently, there is no effective method to study the slurry fracturing mechanism of shield tunneling. This paper presents a numerical simulation method of shield tunneling slurry fracturing based on the extended finite element method (XFEM). The risk of slurry blow-out in shield tunnel crossing reservoir engineering is analyzed. The advantages of the XFEM for simulating crack propagation are fully exploited. Considering the coexistence of tensile and shear failures in soft soils, embedding the combined tensile and shear failure criterion is realized in the XFEM by the secondary development of the ABAQUS extended finite element. Compared with the slurry fracturing test of blind-hole clay samples, the rationality of the simulation method for slurry fracturing in cohesive soil is verified. Through the establishment of the slurry fracturing extension model, the slurry fracturing process of shield tunneling in cohesive soil layer is simulated. The variation law of slurry pressure in the process of fracture extension is studied, and the influence of shield slurry support pressure, overburden thickness, formation shear strength, and slurry viscosity on fracture extension pressure and extension path is analyzed. Based on this numerical simulation method, the risk of slurry blow-out is analyzed in the shield tunneling intersecting the Queshan Reservoir of the Jinan Jiluo Road Crossing the Yellow River Tunnel North Extension Project.

**Keywords:** slurry shield; tunnel excavation face; slurry fracturing; extended finite element method; slurry support pressure; crossing reservoir; slurry blow-out



**Citation:** Han, B.; Yuan, D.; Wang, T.; Wang, Z. Numerical Investigation of Slurry Fracturing during Shield Tunneling under a Reservoir. *Appl. Sci.* **2022**, *12*, 7929. <https://doi.org/10.3390/app12157929>

Academic Editor: Daniel Dias

Received: 19 July 2022

Accepted: 6 August 2022

Published: 8 August 2022

**Publisher's Note:** MDPI stays neutral with regard to jurisdictional claims in published maps and institutional affiliations.



**Copyright:** © 2022 by the authors. Licensee MDPI, Basel, Switzerland. This article is an open access article distributed under the terms and conditions of the Creative Commons Attribution (CC BY) license (<https://creativecommons.org/licenses/by/4.0/>).

## 1. Introduction

The slurry shield method is widely used in the excavation of tunnels in soft soil and composite strata, especially for large-diameter underwater tunnel projects in soft soil [1]. Under complex engineering conditions such as weak stratum, shallow tunnel depth, and rich groundwater, the slurry shield balances the water and soil pressure on the tunnel excavation face by providing slurry support pressure, so as to maintain a safe and efficient tunnel excavation environment. Therefore, the core problem of shield excavation construction is to ensure the stability of the excavation face [2]. Reasonable setting of the shield slurry support pressure is key to realize stable control of the excavation face. However, in the face of the increasing number of large-diameter shallow-covered

underwater shield tunnel projects, it is difficult to reasonably set the support pressure. Improper control of the support pressure will lead to instability of the excavation face, resulting in the destruction of the soil above and in front of the shield, thereby causing engineering accidents. When the slurry support pressure of the shield tunneling is too small, the tunnel excavation face will collapse, causing the soil in the front to pour into the shield, resulting in active instability and failure of the excavation face of the shield tunnel [3,4]. When the shield slurry support pressure is too large, the shield slurry will fracture the stratum above the excavation face front, and the resulting slurry fracturing cracks extend to the surface. When the fracturing develops into a crack channel from the excavation face to the surface, shield slurry will gush out from the surface, known as shield slurry blow-out. Shield slurry blow-out will cause dangerous situations, such as the escape of slurry support pressure and the backflow of overlying water, resulting in passive instability and damage to the excavation face of the shield tunnel [5,6]. The active and passive instability of the excavation face can easily cause accidents such as shield machine downtime, damage, and tunnel collapse. Especially when the shield tunnel passes through water such as rivers, lakes, and seas, construction of the shield tunnel is faced with the situation of shallow covering soil and high water pressure. Slurry blow-out may cause water inrush accidents in the shield tunnel. When the shield tunnel passes through a large drinking water reservoir, shield slurry blow-out will inevitably pollute the drinking water source and endanger public water safety. Therefore, the requirements for preventing the occurrence of shield slurry blow-out are higher when the shield tunnel passes through a domestic water reservoir.

The key contradiction in setting the support pressure of shield tunnels is that it is necessary to provide enough support pressure to resist the water and soil pressure on the excavation face of the tunnel; at the same time, it is necessary to avoid excessive support pressure, which will cause slurry fracturing on the excavation face of the slurry blow-out [7]. Especially for large-diameter shallow-buried tunnels, the relatively low thickness of overburden and the larger shield diameter aggravate this contradiction, making it more difficult to determine the reasonable range of shield excavation face support pressure. In order to predict the active instability failure of the shield tunnel excavation face, many theoretical models and results have been produced in existing research [8–11]. However, there are few theoretical studies on the passive instability of slurry fracturing on the excavation face of shield tunnels.

The research on the slurry fracturing phenomenon of shield tunnels originated from the Tokyo Bay Subsea Tunnel Project in Japan. The phenomenon of shield slurry fracturing mainly includes two basic processes: fracture initiation and crack extension [12]. Mori and Yanagisawa et al. studied the fracture initiation through slurry fracturing laboratory tests of hollow cylindrical clay samples, and proposed some calculation methods to describe the initiation pressure of clay bodies [13–15]. Marchi et al. believed that under the action of slurry pressure, both shear and tensile failure may cause formation fracturing, which largely depends on the properties of soil [16]. Clay strata are more prone to slurry fracturing than sand strata. Wang et al. analyzed the influence of soil strength and slurry viscosity on the fracturing pressure through the triaxial slurry fracturing test of blind-hole specimens [17]. In the current research results, the initiation pressure of slurry fracturing is studied through the mechanical test of geotechnical samples. However, these tests cannot explore the extension process of slurry fracturing in shield tunneling. In order to study the extension process of slurry fracturing in shield tunneling, Yuan and Liu et al. observed the extension of slurry fracturing through the shield model test and field slurry fracturing test, respectively [6,12]. The characteristic laws of the slurry fracturing extension pressure and the extension shape of the split fracture are obtained. Due to the size limitation in the model test of slurry fracturing in shield tunneling, it is difficult to fully capture the occurrence and development process of slurry fracturing. In the field, slurry fracturing tests are observed by manual excavation; the observation process may cause some disturbance to the fracturing surface and implementation is extremely difficult. Jin et al. established a simplified theoretical

model to study the slurry fracturing of shield tunneling [18]. The establishment of the theory is based on a summary of existing experimental laws, and the extension details of shield slurry fracturing are simplified to a certain extent. The phenomenon of shield slurry fracturing occurs in the formation and has strong concealment; it is difficult to directly observe the specific fracturing process. In the influence scope of shield tunnel construction, the stratum mechanics state at the location where slurry fracturing occurs is very complicated. At the same time, it is very important to study the slurry fracturing extension to prevent slurry blow-out in shield tunneling. At present, there is no effective method to study the shield slurry fracturing extension process; therefore, a numerical method was adopted in this paper.

Shield slurry fracturing is a hydraulic cracking phenomenon in soft soil, caused by shield tunnel excavation. In terms of physical mechanism and mechanical behavior, shield slurry fracturing is highly similar to hydraulic fracturing. The key to studying them lies in how to describe the propagation process of the crack tip. At present, there are many research methods on crack propagation [19,20]. A large part of the research results of fracture extension are carried out under the background of hydraulic fracturing. Hydraulic fracturing is a widely used stimulation measure for oil and gas wells, and has quickly become a hot spot in computational mechanics with the “shale gas revolution” in the United States. Hydraulic fracturing is often used in rock formations to increase production. Fracture mechanics theory is usually used to analyze the hydraulic fracturing behavior of rock, a brittle material [21,22]. The failure of soft soil is generally shear failure. Although there are some differences between hydraulic fracturing in rock and soft soil, the existing related research can also provide some reference in numerical simulation analysis methods.

With the development of computing technology, numerical analysis has become a powerful tool for the study of hydraulic fracturing. Although hydraulic fracturing simulation in rock and soil mass is a very difficult problem, there are many numerical methods for hydraulic fracturing simulation due to high attention. Simulation of the hydraulic fracturing process usually involves four processes: (i) mechanical deformation, induced by fluid pressure on fracture surfaces, (ii) fluid flow within the fracture, (iii) fracture propagation, and (iv) coupling of seepage and stress in the computational domain around the fracture [23]. At present, algorithms related to hydraulic fracturing or fracture propagation can be mainly divided into the following categories: the finite element method (FEM) [24], the extended finite element method (XFEM) [25], the discrete element method (DEM) [26], the displacement discontinuity method (DDM) [27], the boundary element method (BEM) [28], etc. Each method has its own advantages and disadvantages. It is necessary to choose the appropriate method according to the application scenario. Among these methods, XFEM has the advantage of high solution accuracy and allows cracks to expand arbitrarily within the element. XFEM overcomes a major challenge in modeling fractures with conventional FEM, by allowing the presence of discontinuities in an element and enriching displacement degrees of freedom. In addition, XFEM can be extended to model hydraulic fracture growth in porous materials by introducing additional pore pressure degrees of freedom to the elements [29]. The XFEM method can be applied to the theory of fracture mechanics well, and is often used to analyze the hydraulic fracturing of rocks [30,31]. When focusing on the propagation path of hydraulic fracturing in rock and soil under a complex stress state, XFEM has good applicability and application potential. At present, XFEM has not been applied to the analysis of shield slurry fracturing.

According to current research, the phenomenon of slurry fracturing in shield tunneling occurs in soft soil layers and is difficult to observe. Simplified theoretical models and model tests have difficulty describing the occurrence process of slurry fracturing, due to the complex stress on the stratum above the shield excavation front. The history of using numerical simulation methods in the field of rock hydraulic fracturing is relatively short. Slurry fracturing of shield tunnels in soft soil is different from rock hydraulic fracturing in terms of failure mechanism and scale. The XFEM numerical simulation method should be a powerful tool to study the slurry fracturing of shield tunneling, but there is no

relevant research at present. A better description of shield slurry fracturing in soft soil is very important, to prevent slurry blow-out and to ensure construction safety. This paper takes the Jinan Jiluo Road Crossing the Yellow River Tunnel North Extension Project, to be built in China and intersecting the Queshan reservoir, as the research object. The purpose is to analyze the risk and prevention methods of slurry blow-out caused by slurry fracturing during shield tunnel construction under the reservoir. Based on the extended finite element method (XFEM), the secondary development of the ABAQUS extended finite element was carried out, and the embedded tension-shear combined failure criterion was realized. Through the establishment of the slurry fracturing extension model, the slurry fracturing process of shield tunneling in sticky soil layer is simulated, the variation law of fracture slurry pressure in the process of fracture extension is studied, and the influence of shield slurry support pressure, overburden thickness, formation shear strength, and slurry viscosity on fracture extension pressure and extension path are analyzed. According to the numerical analysis results, suggestions for preventing slurry blow-out in the construction of shield tunnel crossing reservoirs are put forward.

## 2. Numerical Method

Based on the idea of unit decomposition, the extended finite element method (XFEM) is proposed to deal with the discontinuous displacement field, by introducing an enhanced shape function basis with discontinuous properties into the traditional finite element displacement interpolation function, to represent the discontinuity of the displacement field [32]. This method can not only solve the discontinuity of the hydraulic field, but also simulate the fluid flow between the fractures on the fracture surface under the action of hydraulic pressure, so as to realize the simulation of hydraulic fracturing of rock and soil. Using the XFEM to simulate crack development has the following three advantages: (i) it does not require special meshes to achieve geometric discontinuities, (ii) cracks can propagate within the element and the crack surface does not need to coincide with the element boundary, and (iii) the initiation and propagation of discrete cracks along arbitrary paths can be simulated without refilling the bulk material. Since the fracture is mesh-independent, no remeshing is required as the fracture spreads. Using the XFEM to study rock and soil cracks can greatly improve the calculation speed [33]. In this section, some key aspects of this numerical method are briefly described.

### 2.1. Introduction of Node Enhancement Function

In order to realize the simulation of the crack, the XFEM introduces the displacement enhancement function, including the conventional node deformation function and the enhancement function describing the displacement mutation at the crack [34]. The displacement vector function containing the displacement enhancement component can be expressed as:

$$\mathbf{u} = \sum_{I=1}^N N_I(x) \left[ \mathbf{u}_I + H(x)\mathbf{a}_I + \sum_{\alpha=1}^4 F_{\alpha}(x)\mathbf{b}_I^{\alpha} \right] \quad (1)$$

where  $\mathbf{u}$  is the approximation of a displacement vector,  $N_I(x)$  is the usual nodal shape function,  $\mathbf{u}_I$  is the nodal displacement vector describing continuous deformation in finite element analysis,  $\mathbf{a}_I$  is the displacement vector of the reinforcement nodes on both sides of the crack surface,  $H(x)$  is the jump function across the fracture surfaces,  $\mathbf{b}_I^{\alpha}$  is the displacement vector of the reinforcement node at the crack tip, and  $F_{\alpha}(x)$  is the asymptotic crack-tip function. The three terms on the right side of Equation (1) are used to describe the displacement of all nodes in the model, capture the displacement discontinuity between the fracture surfaces, and the displacement of the crack tip.

The jump function  $H(x)$  can be given by Equation (2). It has a unit value and changes sign as it passes through the crack, while conveying discontinuity on the fractured surface.

$$H(x) = \begin{cases} 1, & \text{if } (x - x^*) \cdot \mathbf{n} \geq 0 \\ -1, & \text{otherwise} \end{cases} \quad (2)$$

where  $x$  is the Gaussian node,  $x^*$  is the point on the crack closest to the Gaussian node  $x$ , and  $\mathbf{n}$  is the unit outer normal vector at point  $x^*$  on the crack.

The crack tip enhancement function  $F_\alpha(x)$  can be expressed as:

$$\{F_\alpha(r, \theta)\}_{\alpha=1}^4 = \left[ \sqrt{r} \sin \frac{\theta}{2}, \sqrt{r} \cos \frac{\theta}{2}, \sqrt{r} \sin \theta \sin \frac{\theta}{2}, \sqrt{r} \sin \theta \cos \frac{\theta}{2} \right] \quad (3)$$

where  $(r, \theta)$  is the polar coordinate system with the crack tip as the origin and  $\theta = 0$  is the direction tangent to the crack. Belytschko and Black give more detailed information on XFEM research results [35].

### 2.2. Unit Cracking Principle

To represent the discontinuity of the cracked element, the elements of the enriched region introduce virtual nodes superimposed on the original real nodes. When the element under load reaches the threshold set for element failure, the element node and the virtual node are separated to produce cracks, and the real nodes on one side of the crack surface on the penetrating cracked element are combined with the virtual nodes on the other side to form a "unit". Figure 1 illustrates the crack propagation.  $a'$ ,  $b'$ ,  $c'$ , and  $d'$  are virtual nodes superimposed with conventional finite element nodes  $a$ ,  $b$ ,  $c$ , and  $d$ , respectively. After the unit fails to form a crack surface that penetrates the unit, a new "unit" is formed as follows:  $a$ ,  $b$ ,  $c'$ , and  $d'$  and  $a'$ ,  $b'$ ,  $c$ , and  $d$ . Of course, the failed real elements in the finite element model are not deleted, but the failed elements do not participate in the rest of the numerical calculation process.

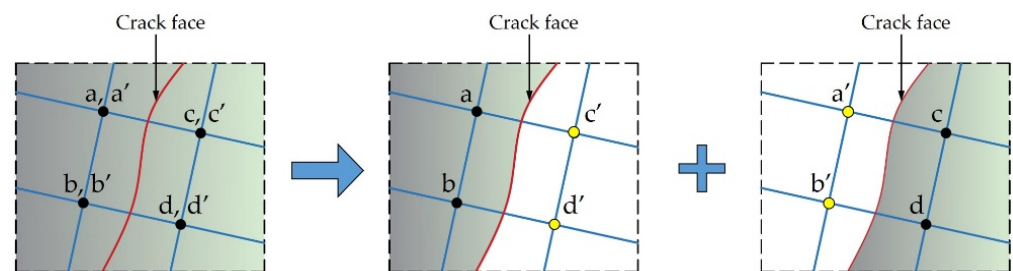


Figure 1. Virtual node and formation of new elements as crack propagates.

To simulate water pressure, additional virtual nodes with pore pressure degrees of freedom were introduced at the edge nodes of each enriched element to simulate fluid flow within the surface of the cracked element. Further, additional virtual nodes are combined with virtual nodes superimposed on the original real nodes to represent the discontinuities in displacement and fluid pressure in the rupture element. A virtual node on an enrichment cell is only activated when a fracture intersects the enrichment cell's boundary. The flow pattern of fracture fluid in the fracture unit is illustrated in Figure 2.

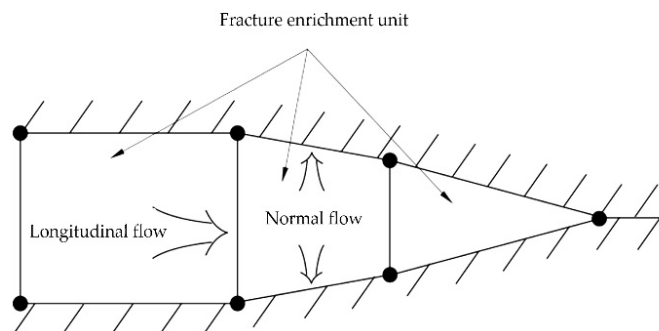


Figure 2. Flow pattern of fluid in fracture.

Assuming that the fluid is incompressible, in order to maintain continuity of the fluid flow, the constitutive response of the fluid flow on the crack surface of the damaged element

includes the tangential flow of fluid on the crack surface and normal fluid loss through the crack surface. The fluid pressure between the fissures acts on the fissure surface, causing the element to have traction separation behavior, thus realizing the simulation of slurry fracturing propagation [36].

The tangential flow at the fracture surface can be modeled using either Newtonian or power models. When the Newton model is used, the calculation formula of the flow density vector of the fluid is as follows:

$$Q = -k_t \nabla p \tag{4}$$

where  $Q$  is the fluid displacement in the fracture,  $k_t$  is the tangential flow coefficient, which is used to describe the frictional resistance of fluid flow, and  $\nabla p$  is the pressure gradient on the fracture surface.

The normal flow of fluid on the crack surface can be achieved by defining the fluid loss coefficient of the material in the XFEM. This coefficient describes the relationship between the pressure difference and the flow velocity between the virtual nodes of the fracture element and the fracture surface; that is, the flow velocity of the fracture surface after the action of the permeable layer is considered, as illustrated in Figure 3.

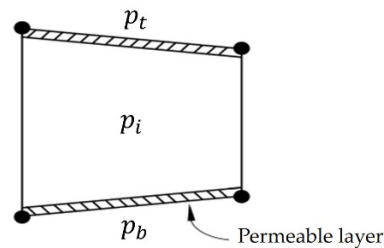


Figure 3. Permeable layer of the fracture surface.

The normal flow velocity of the fluid can be calculated from Equations (5) and (6):

$$q_t = c_t(p_i - p_t) \tag{5}$$

$$q_b = c_b(p_i - p_b) \tag{6}$$

where  $q_t$  and  $q_b$  are the flow rates of the interstitial fluid above and below the fracture, respectively,  $p_i$  is the pressure at the virtual node at the boundary of the ruptured element, and  $p_t$  and  $p_b$  are the pore water pressures at the upper and lower surfaces of the ruptured element, respectively.

### 2.3. Damage Evolution Criterion

The damage evolution law describes how the bond stiffness decreases after the element satisfies the initial damage criterion. The damage evolution is determined by introducing the damage variable  $D$ . The element’s normal and tangential stress components affected by damage are expressed as follows:

$$t_n = \begin{cases} (1 - D)T_n, & T_n \geq 0 \\ T_n, & T_n < 0 \end{cases} \tag{7}$$

$$t_s = (1 - D)T_s \tag{8}$$

$$t_t = (1 - D)T_t \tag{9}$$

where  $D$  is the damage variable, which represents the average damage value between two cracks; its value varies between 0 and 1.  $t_n$ ,  $t_s$ , and  $t_t$  are the normal stress vector  $t$  and the two tangential stress components, respectively.  $T_n$  is the normal stress component of the force-bearing element under linear elastic conditions, and  $T_s$  and  $T_t$  are the first and second tangential stress components of the force-bearing element, respectively. If multiple initial

damage criteria are defined in the self-defined damage criterion, each damage criterion needs to define the response damage evolution law [37].

#### 2.4. Embedding of Tension-Shear Fracture Criterion

There are six fracture criteria in the ABAQUS extended finite element: maximum principal stress, maximum principal strain, maximum nominal stress, maximum nominal strain, secondary nominal stress, and secondary nominal strain [38]. These six fracture criteria are tensile failure; that is, failure will not occur under compression. However, the failure of soft soil layers is mostly shear failure. In order to use the extended finite element to simulate the soft soil layers failure more realistically, it is necessary to embed the shear fracture criterion into the extended finite element through secondary development. The fracture criterion of the ABAQUS extended finite element allows users to customize the fracture criterion through subprograms, which provides the possibility to realize the embedding of shear fracture. Since both shear and tensile failure of soil may occur under different stress states, the newly defined fracture criterion should include both tensile and shear failure. As a relatively mature and perfect shear failure criterion, the Mohr-Coulomb failure criterion has been widely used in the shear failure of rock and soil mass. Based on the basic principle of the Mohr-Coulomb failure criterion, this paper writes its failure principle into the newly defined fracture criterion through a subroutine, and the tension failure criterion adopts the maximum principal stress criterion. Figure 4 illustrates the flow chart of the unit from an initial state to failure under the newly defined failure criterion.

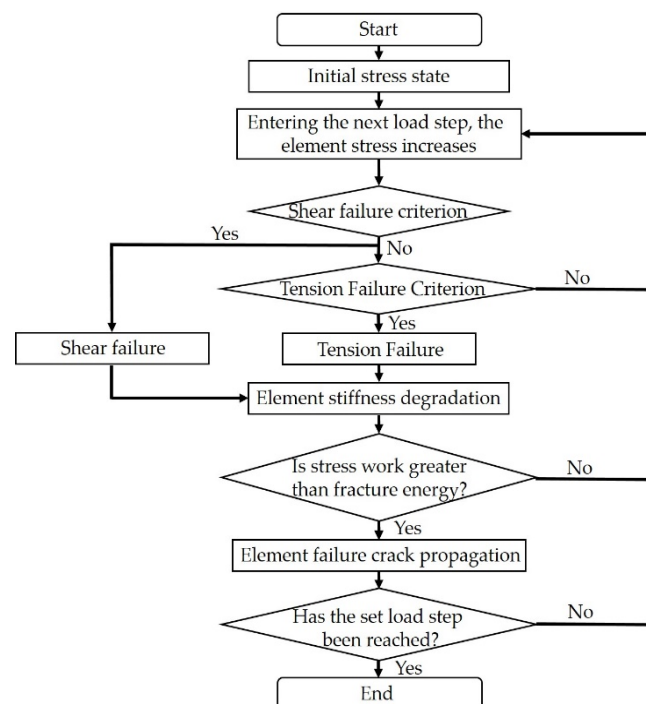


**Figure 4.** Process of tension-shear fracture criterion.

### 3. Verification of Numerical Solution

In order to study shield slurry fracturing, Wang et al. designed a laboratory hydraulic fracturing device, and used blind-hole samples to analyze the influencing factors of clay slurry fracturing, including the soil's unconfined compressive strength, slurry viscosity, loading conditions, etc. [17]. The objective of this section is to verify the capabilities of this method in modeling shield slurry fracturing in clay formations. To this end, the laboratory experiment reported by Wang et al. is numerically duplicated. The XFEM method described in this paper is used to model and calculate the slurry fracturing of the blind-hole samples, and then compared and verified with the test data.

### 3.1. Blind-Hole Samples Model Setup

Modeling is based on the blind-hole cylindrical samples involved in Wang's study. Since the sample is an axisymmetric body, a two-dimensional plane strain model is established by taking its central axis section. The specific dimensions of the model are provided in Figure 5.

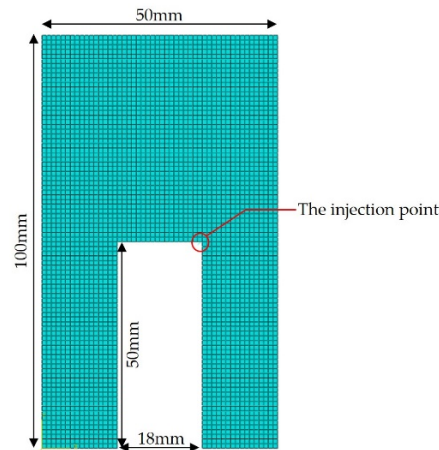


**Figure 5.** Model size.

The slurry injection point is preset at the upper right corner of the blind-hole. Since the initial fracture needs to be preset when using the extended finite element to simulate slurry fracturing, a fracture with a length of 0.1 mm is preset. With reference to the angle of the fracture surface of the samples in the samples fracturing test, the preset crack angle is set to  $45^\circ$ . The injection rate of slurry is 1 mL/s, which is consistent with the test. The established sample model is meshed with node elements, and the grid size is 0.5 mm. The mesh type is plane strain pore compression integral units (CPE4RP). The preset cracks use truss elements, and the mesh size is also 0.5 mm.

Wang et al. measured the relevant parameters of the sample in detail in the slurry fracturing test of the blind-hole sample. In order to compare the simulation results with the test results, the parameters set by the modeling in this paper are selected according to the parameters of the test samples [17]. The specific mechanical parameters of the samples in the study are provided in Table 1. Among the parameters found in the list, type I and type II fracture energies are calculated by the formula Equations (10) and (11).

$$G_I = \frac{K_{IC}^2}{E} \quad (10)$$

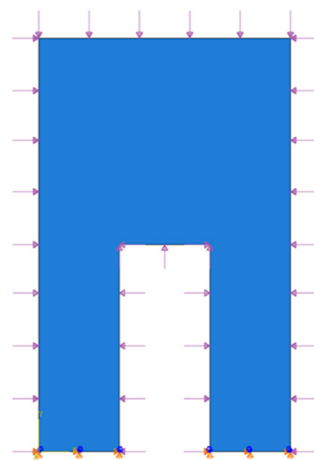
$$G_{II} = \frac{K_{IIC}^2}{E} \quad (11)$$

where  $K_{IC}$  and  $K_{IIC}$  is the fracture toughness of type I and type II, respectively, and  $E$  is the elastic modulus.

When setting the model displacement boundary conditions, set the bottom as a fixed constraint. When setting the stress boundary conditions of the model, the normal stress perpendicular to the boundary is applied to the inner and outer boundaries of the model, and stress is the confining and axial pressure in the test. The boundary conditions of the model are provided in Figure 6. The initial saturation defaults to 1. The initial void ratio is 0.1. The initial pore pressure is 0 MPa. At the same time, define the amplitude curve and set it to slowly increase the injection speed for the first 10 s to prevent shock fluctuations.

**Table 1.** Model Mechanical Parameters.

Parameter	Value
Elastic modulus $E$	75 MPa
Poisson's ratio $\mu$	0.22
Cohesion $c$	0.375 MPa
Internal friction angle $\varphi$	14°
Tensile strength $\sigma_t$	0.13 MPa
Type I fracture energy $G_I$	0.021 MPa·mm
Type II fracture energy $G_{II}$	0.045 MPa·mm
Penetration $k$	$1 \times 10^{-6} \text{ m}^2$
Void ratio $e$	0.1
Filter loss coefficient	$1 \times 10^{-14} \text{ m}^2 \cdot \text{s} / \text{kg}$
Pore flow viscosity coefficient	$0.001 \text{ m}^2 \cdot \text{s} / \text{kg}$

**Figure 6.** Model loading condition settings.

The numerical simulation process of sample slurry fracturing includes two analysis steps: (i) ground stress balance analysis, which uses geometric nonlinear and asymmetric equations to solve; at this stage, an initial stress field is formed and the initial deformation is zeroed out, and (ii) soil analysis, which simulates the slurry injection process and continues to inject slurry at preset fractures until the fracture penetrates the model.

### 3.2. Analysis of Calculation Results and Comparative Validation

During the slurry injection simulation, the slurry pressure at the injection point can be monitored in real-time. Taking the confining pressure of 0.2 MPa and the axial pressure of 0.2 MPa in the model test as an example, the change curve of slurry pressure during the grouting process is provided in Figure 7. It can be observed from this curve that the slurry pressure gradually increases with the injection of slurry, and the slurry pressure drops sharply after reaching the peak value. The peak value is the crack initiation pressure (0.45 Mpa) of the sample fracturing. The crack initiation pressure of the sample is significantly greater than the confining pressure. Under the action of higher triaxial stress, the clay sample exhibits certain brittle characteristics, and the failure develops so quickly that it is difficult to observe. The sudden drop in slurry pressure indicates that the fracture penetration process is extremely rapid (0.73 s). It is almost impossible to observe the slurry fracturing propagation process of the sample during the test. This simulation calculation result is consistent with the slurry fracturing test phenomenon of blind-hole samples described in the test study.

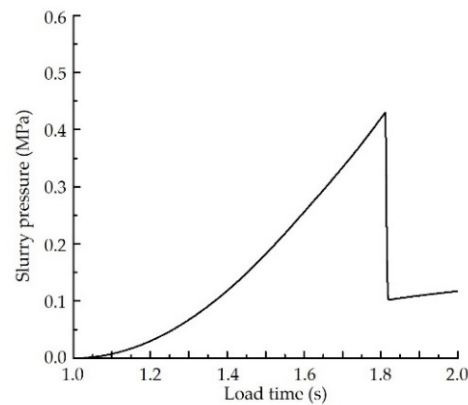


**Figure 7.** Injection point slurry pressure monitoring.

The pressure distribution of the slurry fracture surface is provided in Figure 8. It can be found that the distribution of slurry pressure on the entire fracture surface is basically the same; this is because the viscous resistance of slurry is small and the size of the sample is relatively small, so there is no obvious pressure gradient in the direction of the entire fracture depth. The fracture morphology of the model can be found in Figure 8. By comparing with the damaged sample (as illustrated in Figure 9) given in the test study [17], it can be observed that the fracture surface morphology obtained by the simulation is basically consistent with the experimental results. The comparative results demonstrate the feasibility of the XFEM-based slurry fracturing simulation method. The angle between the failure surface of slurry fracturing and the confining pressure is about  $45^\circ$ , and the overall failure of the clay sample demonstrates shear failure characteristics.

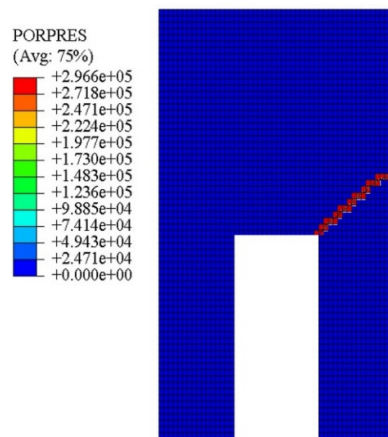


**Figure 8.** Pressure cloud diagram of fracture surface (unit: Pa).



**Figure 9.** Fracture morphology of the samples damaged in slurry fracturing test [17].

It can be observed from the previous simulation examples that the XFEM method proposed in this paper to simulate slurry fracturing can obtain a failure shape that is more consistent with the test samples. In order to verify the accuracy of the simulation calculation results of the fracture initiation pressure, the test conditions under different confining pressures were simulated, and the calculation results were compared with the test results from Wang et al. [17]. According to the setting of the confining pressure in the tests, 6 working conditions are set for the confining pressure when the axial pressure is 0.35 MPa. The fracturing pressure values of numerical calculation results and test results are provided in Table 2. It can be observed that the error of the fracture initiation pressure obtained by simulation under different confining pressures is basically within 5%, compared with the test results, which verifies the accuracy of the numerical simulation results.

**Table 2.** The setting of working conditions and fracture initiation pressure simulation results.

Condition Number	Axial Pressure (MPa)	Confining Pressure (MPa)	Pressure Simulation Value (MPa)	Pressure Test Value (MPa) [17]	Error
1	0.35	0.2	0.36	0.382	−5.76%
2	0.35	0.3	0.45	0.457	−1.53%
3	0.35	0.4	0.58	0.557	4.13%
4	0.35	0.5	0.63	0.652	−3.37%
5	0.35	0.6	0.75	0.735	2.04%
6	0.35	0.7	0.83	0.841	−1.31%

The simulation results of the failure shape of the specimens under different confining pressures are provided in Figure 10. As can be observed from the figure, the fractures of the specimen tend to be vertical when the confining pressure is less than the axial pressure; the fractures of the specimen tend to be horizontal when the confining pressure is greater than the axial pressure. The slurry fractures are deflected in the direction of the maximum principal stress.

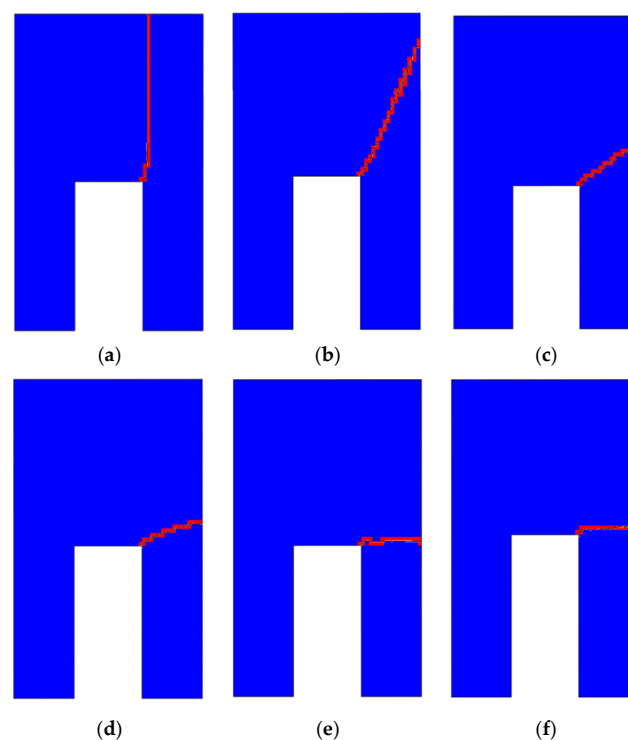


**Figure 10.** Fracturing extension path simulation results of the samples under different confining pressures. (a) 0.2 MPa; (b) 0.3 MPa; (c) 0.4 MPa; (d) 0.5 MPa; (e) 0.6 MPa; (f) 0.7 MPa.

The research conclusions of Mori et al. suggest that there is a linear relationship between the unconfined compressive strength of cohesive soil and the slurry fracturing pressure [13,14]. Based on laboratory tests of cylindrical samples with through boreholes, they proposed an empirical formula for estimating the fracturing pressure:

$$P_f = \sigma_3 + \alpha_v q_u \quad (12)$$

where  $\sigma_3$  is the confining stress,  $\alpha_v$  is the coefficient related to the viscosity of the pressurized liquid, and  $q_u$  is the unconfined compressive strength. The influence of shield slurry viscosity on fracturing is more complicated, so  $\alpha_v$  needs to be valued according to experience, which limits the applicability of the formula.

Wang et al. tested the data of different unconfined compressive strengths and slurry fracturing pressures through the slurry fracturing test of blind-hole samples [17]. The same parameters were used to model and analyze the blind-hole samples with different unconfined compressive strengths, and the slurry fracturing pressure was obtained, which was compared with the test data, as illustrated in Figure 11. The calculation results show that the simulated value of slurry fracturing pressure is slightly larger than the test value. This is due to slight errors between the measured and true values of the clay material parameters. Usually, the determination of clay parameters in the laboratory is accurate. The preparation of blind-pored clay samples is relatively difficult, and it is easy to cause tiny defects and affect the strength of the material. Therefore, when the simulation calculation is accurate, the simulated value is often larger than the experimental value. The fitted relationship between unconfined compressive strength and slurry fracturing pressure demonstrates a linear positive correlation trend, illustrating that the XFEM can obtain consistent laws with the sample tests; the results are consistent with the point of view put forward by Mori. The positive correlation between unconfined compressive strength and splitting pressure also reflects the coexistence of tensile and shear failure. The properties of soil have a great influence on the slurry fracturing pressure.

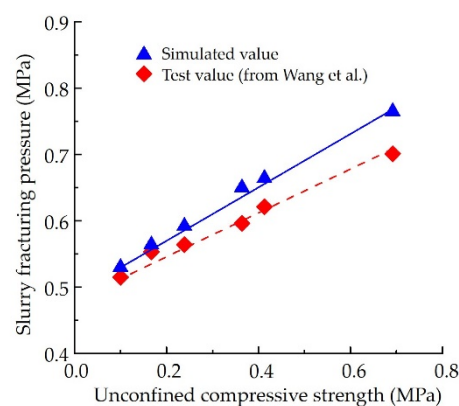


**Figure 11.** Comparison of simulated values and tests of slurry fracturing pressure under different unconfined compressive strengths [17].

Slurry viscosity is also a key factor affecting the slurry fracturing pressure of cohesive soils. The slurry fracturing of the clay blind-hole samples under the condition of slurry with eight viscosities was simulated. The simulation results are compared with the test data, as illustrated in Figure 12. It can be observed that the simulation of slurry fracturing pressure under different slurry viscosities is similar to the test value. The simulated value is always slightly larger than the test value due to the error caused by the disturbance to the samples during the test. The comparison demonstrates that the effect of slurry viscosity on the fracturing pressure is the same. The slurry pressure increases with the increase of slurry viscosity. When the slurry viscosity reaches a certain level (about 25 s), the slurry fracturing pressure will no longer be significantly affected by the slurry viscosity. When the viscosity of the slurry is lower, it is easier for the slurry to reach the tip of the

fracturing crack and transmit the pressure there. With the increase of slurry viscosity, the ability of slurry to transmit pressure to the fracturing tip decreases, leading to an increase in the slurry fracturing pressure of clay samples. When the viscosity of slurry increases to a certain value, it is difficult for slurry to enter the fracturing crack, and the ability to transmit pressure to the fracturing tip does not change significantly. Therefore, the range of controlling the fracturing pressure of clay samples by the viscosity of slurry is limited.

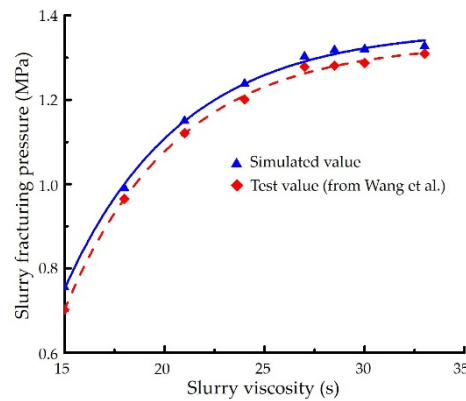


**Figure 12.** Comparison of simulated values and tests of slurry fracturing pressure under different slurry viscosities [17].

Based on the comparison between the above simulation results and the test, the XFEM numerical simulation method proposed in this paper can effectively simulate the failure mode and slurry fracturing pressure of the clay samples. The good correspondence between the numerical and test results verifies that the XFEM is a valid tool for the simulation of shield slurry fracturing. In the following sections, the XFEM method will be used to simulate slurry fracturing during the construction of the shield tunnel crossing the reservoir.

#### 4. Model Setup and Analysis of the Project

##### 4.1. General Project Information and Engineering Conditions

The slurry shield tunnel crossing Queshan Reservoir in this study is designed and constructed for road and subway traffic, which is a sub-project of the Jiluo Road Crossing the Yellow River Tunnel North Extension Project in Jinan, Shandong Province, China. Two slurry-type shield machines are used for the construction of the double-track tunnels, and the distance between the tunnels is about 18 m. The diameter of the shield cutter head used in the project is 15.76 m. After the shield starts to excavate, it will start to cross Queshan Reservoir after excavating about 150 m. The length of the underwater section of the shield tunnel crossing Queshan Reservoir is 1550 m. The buried depth of the shield tunnel in the reservoir area is 13.2 m to 24.5 m. The plan view of the project is provided in Figure 13.



**Figure 13.** Plan view of the project.

Queshan Reservoir is located on the north bank of the Yellow River in Tianqiao District, Jinan City. At present, Queshan Reservoir supplies 60% of the domestic water in the urban area of Jinan, and it is a national first-class water source protection area. The reservoir has been in operation since 2000. Before the reservoir was built, the area was village and farmland. After the residents were relocated, the ground in the area was compacted and a thicker clay layer was laid. According to the geological survey report, the strata for shield tunnel construction in the reservoir area are mainly clay and silty clay. The elevation of the surrounding dam crest of the reservoir is between 31.80 and 33.50 m, which is about 6–8 m higher than the surrounding ground. The highest water level of the reservoir is 30.40 m, which is about 6 m higher than the surrounding ground.

The diameter of the shield used in this project is large, and the risk of shield slurry blow-out is high when crossing the reservoir. According to the experience of the construction unit in the shield tunnel crossing the Yellow River, the existing technology can basically avoid the instability of the excavation face of the deep-buried shield tunnel under the condition of slurry blow-out. However, avoiding the occurrence of shield slurry blow-out is extremely difficult. Small-scale shield slurry blow-out occurred in the shield tunnel crossing the Yellow River near the project site. However, the massive leakage of shield slurry caused by slurry blow-out will pollute the drinking water of the reservoir. The shield slurry blow-out will also damage the seepage-resistant formation at the bottom of the reservoir and increase the leakage rate of the reservoir. Therefore, the risk caused by the shield slurry fracturing in this project is highly concerning to society. The stratum above the bottom of the shield tunnel in this area is mainly cohesive soil, which is more prone to slurry fracturing. In this section, the XFEM method is used to analyze the slurry fracturing phenomenon of the shield tunneling crossing the reservoir.

#### 4.2. Model Setup

It is extremely difficult to model and analyze the entire shield tunnel crossing the reservoir section. In order to obtain valid rules about shield slurry fracturing, it is necessary to select a typical cross-section of this shield tunnel before modeling. The longitudinal section view of the right shield tunnel is provided in Figure 14. The four typical sections marked in Figure 14 were selected for simulation and analysis, according to the characteristics of slurry shield tunneling. The four selected section positions are modeled respectively to analyze the risk of shield slurry fracturing in the project.

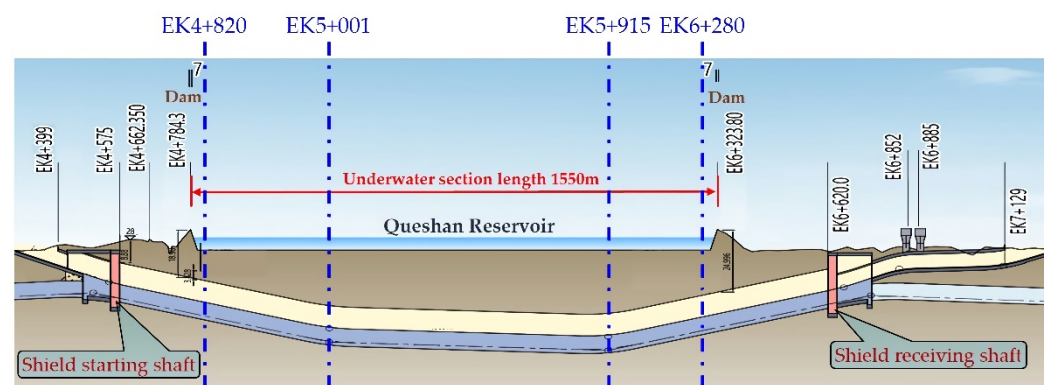


**Figure 14.** The longitudinal section view of the right shield tunnel.

The covering soil thickness and water depth of the four typical sections, according to the preliminary design, are illustrated in Table 3. It can be found that the buried depth of the shield tunnel in this project is shallow. The shallowest position is less than 1 times the tunnel diameter.

**Table 3.** Basic parameters of selected typical section.

Section Location	Covering Thickness (m)	Water Depth (m)
EK4 + 820	13.5	5.1
EK5 + 001	21.4	6.4
EK5 + 915	24.5	6.2
EK6 + 280	17.2	5.5

The analysis process requires modeling and calculation of four typical sections, respectively. Taking the position EK4 + 820 as an example to display the numerical modeling calculation process in this paper, it can be observed from Figure 14 that there is a slope in the design line of the shield tunnel. Since the slope is small and only a small local area is selected for modeling, the tunnel line in the model is simplified to the horizontal direction. The shield tunnel excavation diameter is 15.76 m. The thickness of the covering soil is 13.5 m and the water depth is 5.1 m at the position EK4 + 820. The initial position of the fracturing is located at the vault of the excavation face. The shield slurry injection rate is 1 L/s. In order to improve calculation accuracy, the crack propagation area is densified when dividing the mesh, with a total of 16,543 units. The engineering overview and modeling dimensions of the position EK4 + 820 are provided in Figure 15. The element type is plane strain hole compression integral units (CPE4RP). The bottom of the model has fixed constraints, and the two sides have normal constraints. The top surface of the model is a free surface. Water pressure (51 kPa) is applied to the top of the model in the form of a uniform load. Stress conditions with corresponding soil and water pressures are applied at the tunnel boundary.

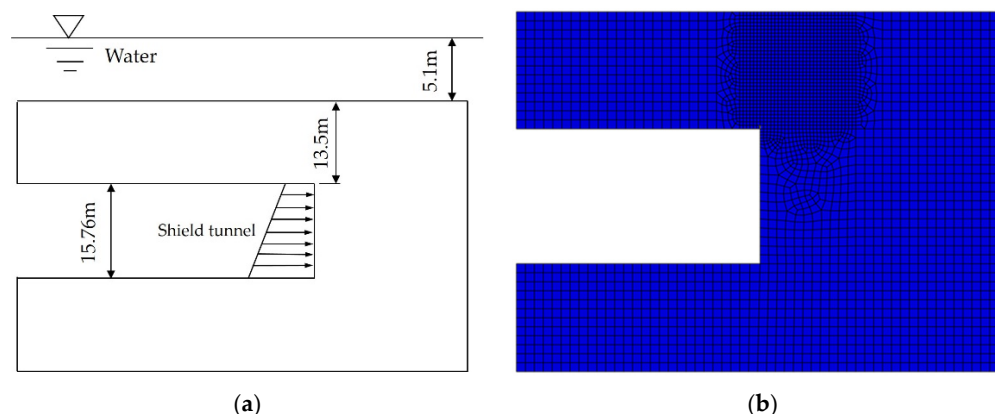


**Figure 15.** The section overview and model of the position EK4 + 820. (a) The section overview; (b) The section model.

According to the geological survey report, the strata where the shield tunnel is located below the reservoir are all cohesive soil strata with similar properties. A single cohesive soil layer was used when modeling the sections. The parameters of the cohesive soil layer are selected according to the geological exploration data and engineering experience, as illustrated in Table 4.

The simulation process of slurry fracturing in shield tunnels is also divided into two stages: earth stress balance and fracturing extension. The initial stress balance is carried out in the in-situ stress balance stage. The loading needs to be kept constant during the fracturing extension stage. The slurry is injected at the preset initial fracture, and the slurry pressurization process continues until the fracture penetrates the model.

**Table 4.** The parameters of the cohesive soil layer at the position EK4 + 820.

Parameter	Value
Elastic modulus $E$	21 MPa
Poisson's ratio $\mu$	0.36
Cohesion $c$	0.013 MPa
Internal friction angle $\varphi$	16.8
Tensile strength $\sigma_t$	0.011 MPa
Type I fracture energy $G_I$	$5.4 \times 10^{-4}$ MPa·mm
Type II fracture energy $G_{II}$	$5.4 \times 10^{-4}$ MPa·mm
Penetration $k$	$1 \times 10^{-6}$ m <sup>2</sup>
Void ratio $e$	0.1
Filter loss coefficient	$1 \times 10^{-14}$ m <sup>2</sup> ·s/kg
Pore flow viscosity coefficient	0.001 m <sup>2</sup> ·s/kg

#### 4.3. Shield Slurry Fracturing Extension Process

Take the section EK4 + 820 as an example to model and analyze the extension process of shield slurry fracturing in the formation. Figure 16 demonstrates the slurry fracturing morphology when the crack tip is at different distances from the tunnel vault during the slurry fracturing extension process. It can be observed that from the initial failure at the top of the excavation face to the complete penetration of the slurry fracturing, the fracturing maintains a stable angle and extends upward obliquely.

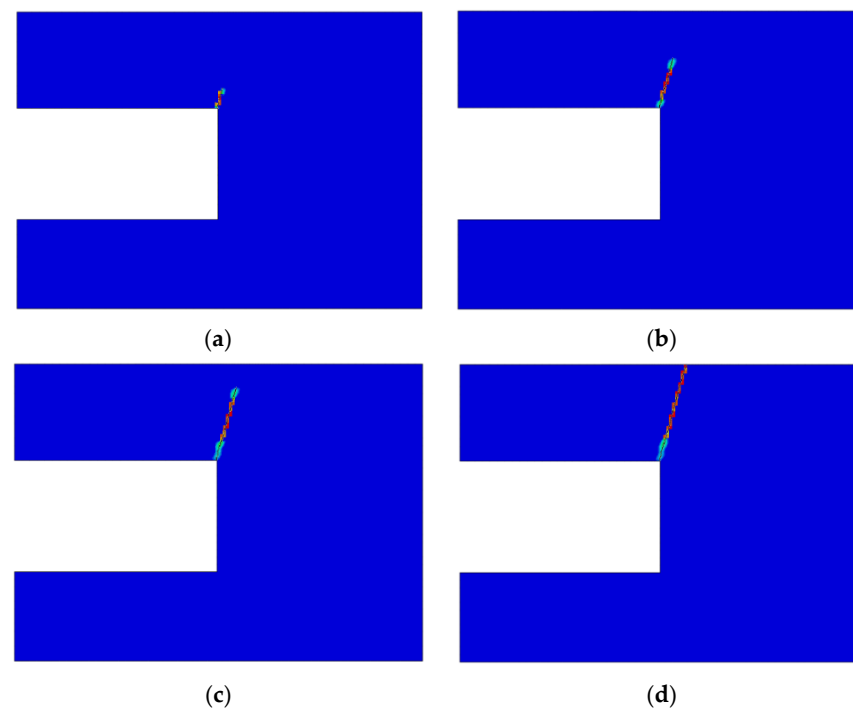


**Figure 16.** The shield slurry fracturing morphology when the fracturing tip extends to different heights (EK4 + 820). (a) 3 m; (b) 6 m; (c) 9 m; (d) 13.5 m.

In the process of slurry injection, the change curve of slurry pressure at the grouting port of the shield excavation face at section EK4 + 820 is provided in Figure 17. With the continuous injection of slurry, the slurry pressure reaches the maximum value when the formation cracks. After that, the pressure value oscillates and decreases, which is due to the increase of slurry pressure in the fracture caused by the injection of slurry when the fracture is not expanding. When the fracture begins to expand, the volume of the fracture increases suddenly, and the slurry pressure in the fracture also decreases sharply. With the continuous replenishment of slurry, the slurry pressure begins to increase again until the

fracture further expands. With the oscillating process of this slurry pressure, shield slurry fracturing spreads to the surface. With the upward expansion of the fracture, the water and soil pressure on the fracture surface becomes smaller and smaller, so the slurry fracturing pressure also gradually decreases.

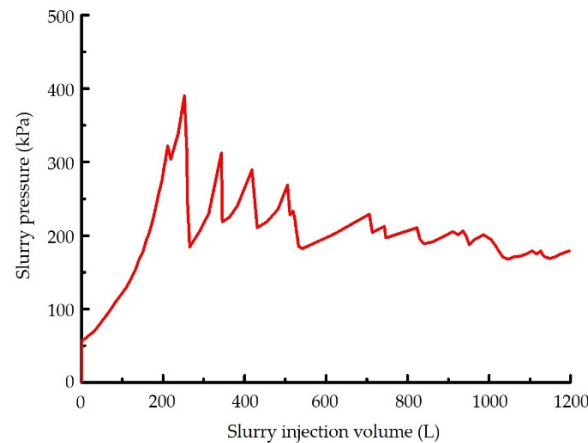


**Figure 17.** Variation of slurry pressure with slurry injection volume (EK4 + 820).

Finally, the slurry pressure at the grouting port on the excavation face of the shield tunnel is stable in the range of about 180 kPa; this is mainly because, after the fracture completely penetrates the overlying soil layer, the tunnel and surface form a communication channel. The slurry pressure at this time will be the same as the water pressure at this position, and the water head height at the grouting port of the excavation face vault is about 18 m. At this time, a shield slurry blow-out occurred on the surface.

In summary, the formation fracturing pressure at section EK4 + 820 is about 0.39 MPa, and the pressure required for the fracture to continue to expand gradually decreases after the initial formation failure occurs.

#### 4.4. Slurry Fracturing Pressure of Different Sections

According to the design characteristics of the tunnel line, four typical cross-sections of the tunnels are selected for modeling and calculation. Figure 18 illustrates the slurry pressure during the formation fracturing process of the four control sections, respectively. The maximum peak value of the pressure curve is the formation fracturing initiation pressure. With the parameters provided in Table 3, it can be observed that the water depth difference of the four sections is small. The initial slurry fracturing pressure of the formation increases with the increase of burial depth. With the increase of buried shield tunnel depth, the maximum length of the slurry fracturing in the formation will also increase. At the same time, the amount of slurry injected will increase with the growth of fracture, which is reflected in the pressure fluctuation curves of different lengths in Figure 18.

When the slurry pressure at each section reaches the peak of the pressure curve, the slurry fracturing begins to extend continuously. In order to prevent slurry from fracturing and extending to slurry blow-out, it is better to take the peak value of the slurry pressure curve as the maximum value of shield slurry support pressure. Due to the error in the control of the shield support pressure, the support pressure of the section at the shallow depth of the tunnel is small and it is more difficult to control. In addition, the slurry fracturing of the section with smaller buried depth spreads faster, and the construction control is more difficult.

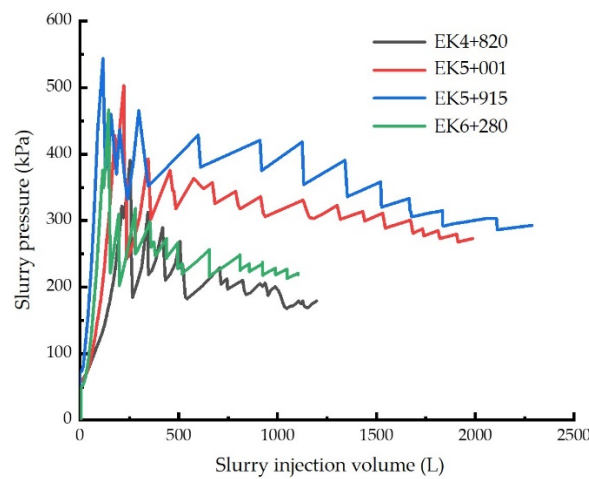


Figure 18. Variation of slurry pressure with slurry injection volume at different sections.

#### 4.5. Upper Limit of Shield Slurry Support Pressure

In the same formation, the slurry fracturing pressure of the shield is generally proportional to the burial depth of the location. In this project, the stratigraphic parameters of the reservoir area are relatively similar. The bottom of the reservoir is relatively flat. The difference in water depth inside the reservoir is small. In the simulation in this section, the two sections EK5 + 001 and EK5 + 915 are selected as the inflection points of the slope change of the shield tunnel line. Based on the upper limit of the support pressure of the four sections illustrated in Table 3, obtained from the simulation, the simplified upper limit of the support pressure of the entire tunnel crossing the reservoir can be obtained, as demonstrated in Figure 19.

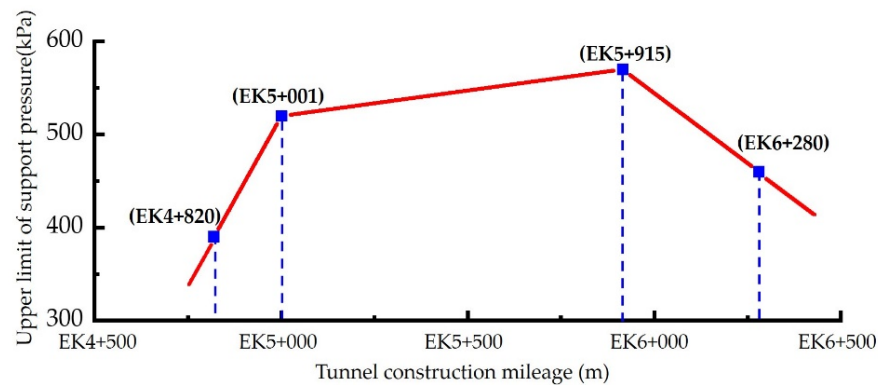


Figure 19. Predicted value of upper limit of shield slurry support pressure in tunnel crossing reservoir section.

The upper limit of the shield slurry support provided in Figure 19 is a reference value only, considering the prevention of slurry fracturing. The purpose is to give advice on support pressure control during the construction of a shield tunnel crossing the reservoir. Since there are few methods to prevent and control the slurry fracturing of the shield, it is more important to accurately set the shield slurry support pressure. From the research in the previous section, it can be observed that increasing the viscosity of slurry can slow down the expansion of fractures. In engineering, the method of increasing the viscosity of slurry can be used to prevent slurry blow-out, improving the tunneling speed of the shield machine after the slurry fracturing occurs. The shield can also drive quickly to seal the fracture opening to prevent the further extension of the fracture. In summary, when the shield tunneling reaches the formation prone to slurry fracturing, it is necessary to adopt the various control methods mentioned above to avoid slurry blow-out. According to the improved XEFM, the shield support pressure upper limit to prevent slurry fracturing

can be obtained in the simulated case study, which can guide the construction personnel to control the shield support pressure value. When the upper limit of the shield support pressure is too small to make it difficult to be controlled during construction, it can be optimized from the perspective of shield tunnel site selection and buried depth design to avoid slurry fracturing.

## 5. Conclusions

Relying on the large-diameter shield tunnel crossing large drinking water reservoir project, this paper uses the XFEM numerical simulation to study the occurrence and extension of slurry fracturing in shield tunnels in cohesive soil layers. Based on the extended finite element method (XFEM), the secondary development of the ABAQUS extended finite element was carried out, and the embedded tension-shear combined failure criterion was realized. The XFEM method was verified by comparing the numerical simulation calculation of the blind-hole samples with the test data. Typical sections of the shield tunnel that cross the reservoir in this project were selected for simulation. The variation law of slurry fracturing pressure in the process of slurry fracturing and propagation is analyzed. The effects of shield slurry support pressure, overburden thickness, formation shear strength, and slurry viscosity on fracture propagation pressure and propagation path were studied. Based on numerical simulation and analysis, the upper limit of the shield slurry support pressure of the shield tunnel crossing the reservoir in this project is briefly given, and the following results are obtained:

- (1) Both tensile and shear failures exist in the slurry fracturing process of the clay formation. The error of the fracture initiation pressure obtained by simulation under different confining pressures is basically within 5%, compared with the test results. After introducing the combined tensile-shear failure criterion, the calculation results of the XFEM method are in good agreement with the test data of slurry fracturing of clay samples.
- (2) The slurry fracturing pressure of cohesive soil increases with the increase of soil stress, unconfined compressive strength, and slurry viscosity. When the slurry viscosity reaches a certain level (about 25 s), the slurry fracturing pressure is no longer significantly affected by the slurry viscosity. The slurry fractures are deflected in the direction of the maximum principal stress.
- (3) The shield slurry fracturing pressure in the same stratum will rise with the increase of tunnel burial and overlying water depths. With the slurry continuously injected, the slurry pressure reaches the peak at the initiation of shield slurry fracturing in cohesive soil layers. The slurry pressure gradually decreases with the extension of the fracture, and the slurry pressure will be equal to the water pressure of the tunnel vault after the fracture penetrates to the surface.
- (4) Precisely controlling the shield slurry support pressure to be less than the upper limit of the support pressure is important to avoid slurry fracturing. Increasing the viscosity of slurry can slow down the expansion of fractures. In the process of shield construction, the proper increase in viscosity of the slurry can slow down the spreading speed of the slurry fracturing. The shield can drive quickly to seal the fracture opening to prevent further extension of the fracture. When the upper limit of the shield support pressure is too small, making it difficult to control during construction, it can be optimized from the perspective of shield tunnel site selection and buried depth design to avoid slurry fracturing.

**Author Contributions:** Conceptualization, B.H. and D.Y.; methodology, B.H. and D.Y.; software, B.H. and T.W.; validation, B.H., T.W. and Z.W.; formal analysis, B.H.; investigation, B.H.; resources, D.Y.; data curation, B.H. and Z.W.; writing—original draft preparation, B.H.; writing—review and editing, B.H. and T.W.; visualization, T.W.; supervision, D.Y.; project administration, D.Y.; funding acquisition, D.Y. All authors have read and agreed to the published version of the manuscript.

**Funding:** This research was funded by the National Natural Science Foundation of China under Grant No. 52008021, and the Key Project of High-speed Rail Joint Fund of National Natural Science Foundation of China under Grant No. U1834208.

**Institutional Review Board Statement:** Not applicable.

**Informed Consent Statement:** Not applicable.

**Data Availability Statement:** The data presented in this study might be available on reasonable request from the corresponding author.

**Acknowledgments:** The authors gratefully thank the reviewers for their great help with the article during the review process. The authors gratefully acknowledge resources and technical support from Jian Chen and Gongbiao Yang, who are affiliated with the China RAILWAY 14TH BUREAU Group Co., Ltd. and China Railway Construction Underwater Tunnel Engineering Laboratory.

**Conflicts of Interest:** The authors declare no conflict of interest.

## References

1. Zhang, F.; Gao, Y.; Wu, Y.; Wang, Z. Face stability analysis of large-diameter slurry shield-driven tunnels with linearly increasing undrained strength. *Tunn. Undergr. Space Technol.* **2018**, *78*, 178–187. [\[CrossRef\]](#)
2. Mollon, G.; Dias, D.; Soubra, A.-H. Rotational failure mechanisms for the face stability analysis of tunnels driven by a pressurized shield. *Int. J. Numer. Anal. Meth. Geomech.* **2011**, *35*, 1363–1388. [\[CrossRef\]](#)
3. Pan, Q.; Dias, D. Three dimensional face stability of a tunnel in weak rock masses subjected to seepage forces. *Tunn. Undergr. Space Technol.* **2018**, *71*, 555–566. [\[CrossRef\]](#)
4. Zhang, C.; Li, W.; Zhu, W.; Tan, Z. Face stability analysis of a shallow horseshoe-shaped shield tunnel in clay with a linearly increasing shear strength with depth. *Tunn. Undergr. Space Technol.* **2020**, *97*, 103291. [\[CrossRef\]](#)
5. Liu, D.; Liu, X.; Han, Y.; Xiong, F.; Liu, R.; Lin, C.; Deng, Z.; Xiao, Y.; Luo, W. Model Test on the Passive Failure of Slurry Shield Tunneling in Circular-Gravel Stratum. *Earth Space Sci.* **2022**, *9*, 17. [\[CrossRef\]](#)
6. Liu, X.; Yuan, D. An in-situ slurry fracturing test for slurry shield tunneling. *J. Zhejiang Univ. A* **2014**, *15*, 465–481. [\[CrossRef\]](#)
7. Liu, X.; Wang, F.; Yuan, D.; Fang, H.; Zhang, S. Range of support pressures for slurry shield and analysis of its influence factors. *Chin. J. Geotech. Eng.* **2019**, *41*, 908–917. (In Chinese) [\[CrossRef\]](#)
8. Min, F.; Zhu, W.; Lin, C.; Guo, X. Opening the excavation chamber of the large-diameter size slurry shield: A case study in Nanjing Yangtze River Tunnel in China. *Tunn. Undergr. Space Technol.* **2015**, *46*, 18–27. [\[CrossRef\]](#)
9. Zhang, F.; Gao, Y.; Wu, Y.; Zhang, N. Upper-bound solutions for face stability of circular tunnels in undrained clays. *Geotechnique* **2018**, *68*, 76–85. [\[CrossRef\]](#)
10. Alagha, A.S.N.; Chapman, D.N. Numerical modelling of tunnel face stability in homogeneous and layered soft ground. *Tunn. Undergr. Space Technol.* **2019**, *94*, 103096. [\[CrossRef\]](#)
11. Dai, C.; Sui, H.; Ma, C. Study on the Ultimate Supporting Force of Shield Excavation Face Based on Anisotropic Strength Theory. *Appl. Sci.* **2020**, *10*, 5222. [\[CrossRef\]](#)
12. Yuan, D.; Luo, W.; Jin, D.; Lu, P. Hydraulic fracturing pressure of concentric double-layered cylinder in cohesive soil. *Front. Struct. Civ. Eng.* **2021**, *15*, 937–947. [\[CrossRef\]](#)
13. Mori, A.; Tamura, M. Hydrofracturing pressure of cohesive soils. *Soils Found.* **1987**, *27*, 14–22. [\[CrossRef\]](#)
14. Mori, A.; Tamura, M.; Fukui, Y. Fracturing pressure of soil ground by viscous materials. *Soils Found.* **1990**, *30*, 129–136. [\[CrossRef\]](#)
15. Yanagisawa, E.; Panah, A.K. Two dimensional study of hydraulic fracturing criteria in cohesive soils. *Soils Found.* **1994**, *34*, 1–9. [\[CrossRef\]](#)
16. Marchi, M.; Gottardi, G.; Soga, K. Fracturing Pressure in Clay. *J. Geotech. Geoenviron.* **2014**, *140*, 04013008. [\[CrossRef\]](#)
17. Wang, T.; Yuan, D.; Jin, D.; Li, X. Experimental study on slurry-induced fracturing during shield tunneling. *Front. Struct. Civ. Eng.* **2021**, *15*, 333–345. [\[CrossRef\]](#)
18. Jin, D.; Ng, Y.C.H.; Han, B.; Yuan, D. Modeling Hydraulic Fracturing and Blow-Out Failure of Tunnel Face During Shield Tunneling in Soft Soils. *Int. J. Geomech.* **2022**, *22*, 06021041. [\[CrossRef\]](#)
19. Chen, Y.; Zuo, J.P.; Li, Z.H.; Dou, R. Experimental investigation on the crack propagation behaviors of sandstone under different loading and unloading conditions. *Int. J. Rock Mech. Min. Sci.* **2020**, *130*, 10. [\[CrossRef\]](#)
20. Li, W.D.; Nhon, N.T.; Huang, J.Z.; Zhou, K. Adaptive analysis of crack propagation in thin-shell structures via an isogeometric-meshfree moving least-squares approach. *Comput. Meth. Appl. Mech. Eng.* **2020**, *358*, 26. [\[CrossRef\]](#)
21. Cherdantsev, N.V. Approach to Constructing a Hydraulic Fracture Trajectory in a Rock Mass Near a Mine Working. *Mech. Sol.* **2020**, *55*, 1372–1391. [\[CrossRef\]](#)
22. Li, W.D.; Nhon, N.T.; Zhou, K. An isogeometric-meshfree collocation approach for two-dimensional elastic fracture problems with contact loading. *Eng. Fract. Mech.* **2020**, *223*, 19. [\[CrossRef\]](#)
23. Kumar, S.; Zielonka, M.; Searles, K.; Dasari, G. Modeling of hydraulic fracturing in ultra-low permeability formations: The role of pore fluid cavitation. *Eng. Fract. Mech.* **2017**, *184*, 227–240. [\[CrossRef\]](#)

24. Wrobel, M.; Papanastasiou, P.; Peck, D. Numerical simulation of hydraulic fracturing: A hybrid FEM-based algorithm. *Int. J. Numer. Anal. Met.* **2022**, *1–26*. [[CrossRef](#)]
25. Sheng, M.; Li, G.; Sutula, D.; Tian, S.; Bordas, S.P.A. XFEM modeling of multistage hydraulic fracturing in anisotropic shale formations. *J. Pet. Sci. Eng.* **2018**, *162*, 801–812. [[CrossRef](#)]
26. Tomac, I.; Gutierrez, M. Micromechanics of hydraulic fracturing and damage in rock based on DEM modeling. *Granul. Matter* **2020**, *22*, 1–17. [[CrossRef](#)]
27. Xie, L.; Min, K.; Shen, B. Simulation of hydraulic fracturing and its interactions with a pre-existing fracture using displacement discontinuity method. *J. Nat. Gas. Sci. Eng.* **2016**, *36*, 1284–1294. [[CrossRef](#)]
28. Behnia, M.; Goshtasbi, K.; Marji, M.F.; Golshani, A. Numerical simulation of crack propagation in layered formations. *Arab. J. Geosci.* **2014**, *7*, 2729–2737. [[CrossRef](#)]
29. Feng, Y.; Gray, K. Modeling of curving hydraulic fracture propagation from a wellbore in a poroelastic medium. *J. Nat. Gas. Sci. Eng.* **2018**, *53*, 83–93. [[CrossRef](#)]
30. Wu, Y.; Wang, Y.X.; Haim, W.; He, S.M.; Li, X.P. Fracture of rocks in the mountains of Southeast Tibet under hydrothermal conditions at different elevations. *Bull. Eng. Geol. Environ.* **2020**, *79*, 4291–4308. [[CrossRef](#)]
31. Huang, J.Z.; Nhon, N.T.; Li, W.D.; Zhou, K. An adaptive isogeometric-meshfree coupling approach for the limit analysis of cracked structures. *Theor. Appl. Fract. Mech.* **2020**, *106*, 14. [[CrossRef](#)]
32. Moes, N.; Dolbow, J.; Belytschko, T. A finite element method for crack growth without remeshing. *Int. J. Numer. Meth. Eng.* **1999**, *46*, 131–150. [[CrossRef](#)]
33. Asferg, J.L.; Poulsen, P.N.; Nielsen, L.O. A consistent partly cracked XFEM element for cohesive crack growth. *Int. J. Numer. Meth. Eng.* **2007**, *72*, 464–485. [[CrossRef](#)]
34. Fries, T.P.; Belytschko, T. The extended/generalized finite element method: An overview of the method and its applications. *Int. J. Numer. Meth. Eng.* **2010**, *84*, 253–304. [[CrossRef](#)]
35. Belytschko, T.; Black, T. Elastic crack growth in finite elements with minimal remeshing. *Int. J. Numer. Meth. Eng.* **1999**, *45*, 601–620. [[CrossRef](#)]
36. Wang, H. Numerical modeling of non-planar hydraulic fracture propagation in brittle and ductile rocks using XFEM with cohesive zone method. *J. Petrol. Sci. Eng.* **2015**, *135*, 127–140. [[CrossRef](#)]
37. Ghaderi, A.; Taheri-Shakib, J.; Nik, M.A.S. The distinct element method (DEM) and the extended finite element method (XFEM) application for analysis of interaction between hydraulic and natural fractures. *J. Petrol. Sci. Eng.* **2018**, *171*, 422–430. [[CrossRef](#)]
38. Duarte, A.P.C.; Saez, A.D.; Silvestre, N. Comparative study between XFEM and Hashin damage criterion applied to failure of composites. *Thin Wall. Struct.* **2017**, *115*, 277–288. [[CrossRef](#)]